FULL PAPER

An Indium-Free Anode for Large-Area Flexible OLEDs: Defect-Free Transparent Conductive Zinc Tin Oxide

Monica Morales-Masis, Fabien Dauzou, Quentin Jeangros, Ali Dabirian, Herbert Lifka, Rainald Gierth, Manfred Ruske, Date Moet, Aïcha Hessler-Wyser, and Christophe Ballif*

Flexible large-area organic light-emitting diodes (OLEDs) require highly conductive and transparent anodes for efficient and uniform light emission. Tin-doped indium oxide (ITO) is the standard anode in industry. However, due to the scarcity of indium, alternative anodes that eliminate its use are highly desired. Here an indium-free anode is developed by a combinatorial study of zinc oxide (ZnO) and tin oxide (SnO_2), both composed of earth-abundant elements. The optimized Zn–Sn–O (ZTO) films have electron mobilities of up to 21 $cm^2 V^{-1} s^{-1}$, a conductivity of 245 S cm^{-1}, and <5% absorptance in the visible range of the spectrum. The high electron mobilities and low surface roughness (<0.2 nm) are achieved by producing dense and void-free amorphous layers as confirmed by transmission electron microscopy. These ZTO layers are evaluated for OLEDs in two anode configurations: i) 10 cm^2 devices with ZTO/Ag/ZTO and ii) 41 cm^2 devices with ZTO plus a metal grid. The ZTO layers are compatible with OLED processing steps and large-area white OLEDs fabricated with the ZTO/grid anode show better performance than those with ITO/grid anodes. These results confirm that ZTO has the potential as an In-free and Earth-abundant alternative to ITO for large-area flexible OLEDs.

1. Introduction

Organic light-emitting diodes (OLEDs) provide unique features such as uniform flat illumination combined with mechanical flexibility that are not attainable in traditional lighting solutions.[1,2] An OLED comprises a multilayer of organic light-emitting materials sandwiched between a hole transport layer and an electron transport layer. These layers are connected to the electrical drivers through electrodes: the anode on the hole injection side and the cathode on the electron injection side. In the so-called "bottom emitting" configuration, the OLED emits light from the anode side of the device.[1,3,4] This anode should therefore have minimal optical absorption losses in the visible to ensure efficient light emission, and it should have minimal sheet resistance (Ω sq^{-1}) for efficient and uniform lateral current injection and hence uniform luminance. In addition, anodes with low surface roughness are required to prevent current leakage and shunting of the devices through the organic active layers. In addition, these should be fabricated at low temperatures (<200 °C) for compatibility with standard flexible substrates, such as polyethylene terephthalate (PET) and naphthalate (PEN) substrates.

Tin-doped indium oxide (ITO) is the leading transparent conducting oxide (TCO) used as the anode for glass-based and flexible OLEDs[1,3,5–8] due to its high conductivity and optical transmittance in the visible range and reasonable surface roughness of 1–2 nm root mean square (RMS). However, ITO, which contains 90 wt% of indium oxide (In_2O_3), is not a sustainable solution for OLED lighting due to the scarcity of indium in the Earth's crust, which results in high cost.[9] Hence, there is a strong interest in developing low-cost alternative compounds to ITO.[10] Aluminum[11] and gallium-doped ZnO[12] OLED anodes have been proposed in literature, however, the poor stability of these materials in oxidizing environments and etchability when in contact with acids restricts their application and large-scale deployment in optoelectronic devices.[13] Several other strategies have been pursued to develop flexible In-free transparent electrodes for OLEDs, such as metal nanowires and networks,[14–16]

Dr. M. Morales-Masis, F. Dauzou, Dr. Q. Jeangros, Dr. A. Dabirian, Dr. A. Hessler-Wyser, Prof. C. Ballif
Ecole Polytechnique Fédérale de Lausanne (EPFL)
Institute of Microengineering (IMT)
Photovoltaics and Thin Film Electronics Laboratory
Rue de la Maladière 71, Neuchatel 2002, Switzerland
E-mail: monica.moralesmasis@epfl.ch
H. Lifka, Dr. D. Moet
TNO/Holst Centre
High Tech Campus 31
5656 AE, Eindhoven, The Netherlands
R. Gierth
Philips GmbH
Innovative Technologies
Research Laboratories
Philipsstr. 8, D-52068 Aachen, Germany
M. Ruske
Philips GmbH
Business Center OLED Lighting
Philipsstr. 8, D-52068 Aachen, Germany

DOI: 10.1002/adfm.201503753

© 2015 WILEY-VCH Verlag GmbH & Co. KGaA, Weinheim

optically transparent thin metal films,[17,18] graphene,[19,20] and polymer conductors.[21] These solutions, although suitable for flexible applications, have not reached the performance and stability of ITO. This, among other reasons including process scalability, has hindered their commercialization.

In this article, we report the development of a zinc tin oxide (ZTO) amorphous compound with optimized optical and conductive properties for application in small-molecule OLED (sm-OLED) flexible lighting. The optimized void-free amorphous ZTO films were fabricated by sputtering deposition, which is a common industrial process that will facilitate upscaling and ITO replacement at the industrial level. The ZTO films were also extremely stable under thermal and acid treatments.[22] Large-area (10 and 41 cm^2) sm-OLEDs were fabricated on these ZTO electrodes, in combination with a Ag thin intermediate layer or a metal grid, and compared to devices fabricated with ITO. The performance figures, i.e., turn-on voltage, luminance, and stability of the OLEDs with ITO and ZTO anodes, were compared and from these measurements it is concluded that ZTO can substitute ITO for large-area OLED lighting applications.

2. Results and Discussion

2.1. Combinatorial Screening of ZTO Compounds by Cosputtering

ZTO films with different Sn/Zn ratios were deposited by cosputtering from SnO_2 and ZnO:Al (2 wt% Al_2O_3) targets. The ZnO:Al and SnO_2 targets were powered by independent radio frequency (RF) supplies (power densities of 2 and 5 W cm^{-2}, respectively). To achieve a compositional gradient, the substrate holder was used in a nonrotation mode. **Figure 1** illustrates the sample configuration for the off-axis cosputtering deposition and, for each sample, shows the Sn/Zn ratio, sheet resistance (R_{sh}), top-view scanning transmission electron microscopy (STEM) bright-field (BF), and high-angle annular dark-field (HAADF) images together with corresponding selected-area electron diffraction (SAED) patterns.

From zones 1 to 5—as shown in Figure 1—the Sn/Zn ratio varies from 23 down to 0.7. Decreasing the Sn/Zn ratio induces a transition from polycrystalline rutile SnO_2 to an amorphous film,

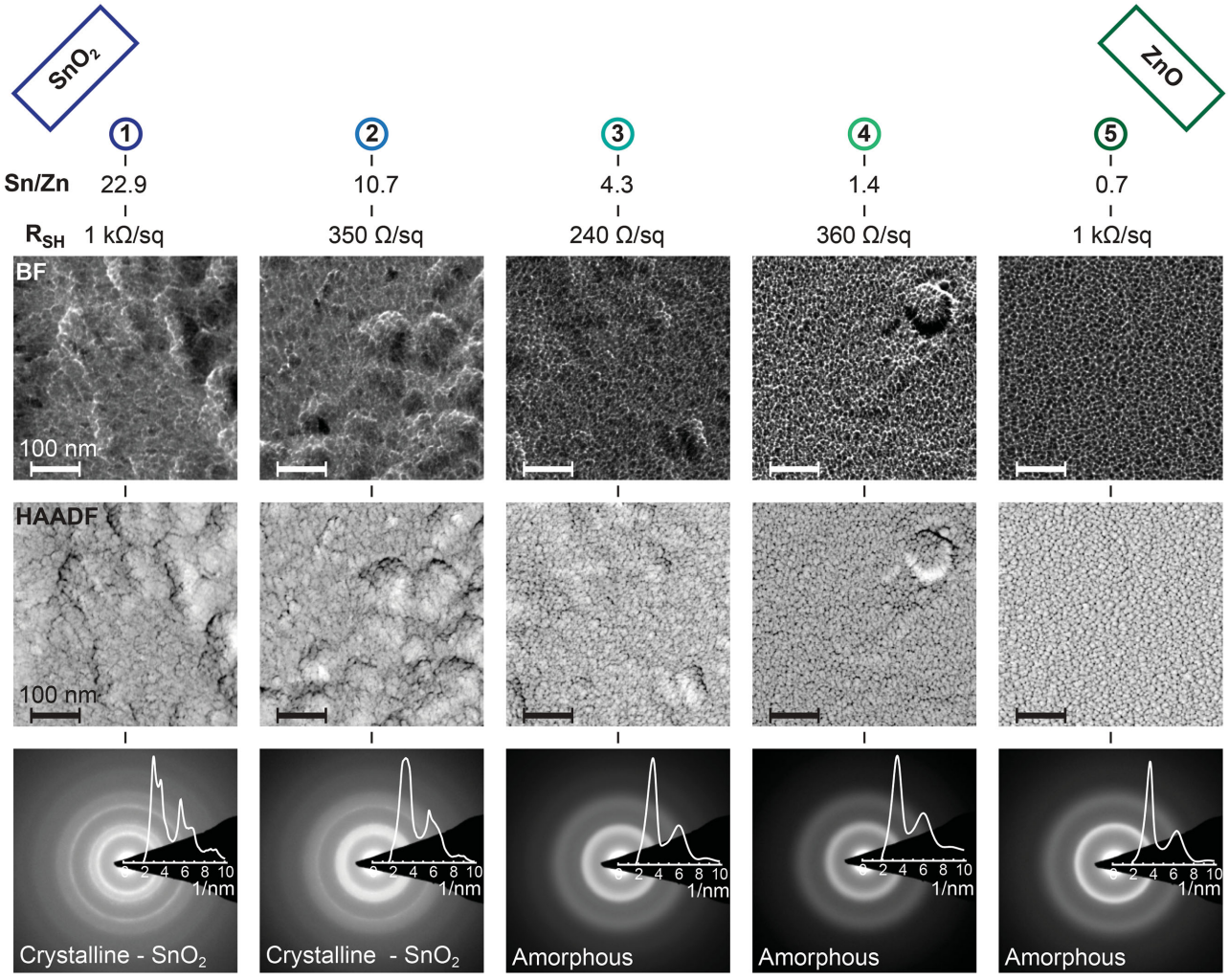

Figure 1. From top to bottom: Sample configuration during cosputtering of SnO_2 and ZnO:Al targets and characterization including Sn/Zn ratio, sheet resistance (R_{sh}), microstructural characterization by STEM bright-field and high-angle annular dark-field images, and SAED patterns along with radial intensity profiles. The thickness of the films decreases progressively from 300 nm in zone 1 to 250 nm in zone 5.

© 2015 WILEY-VCH Verlag GmbH & Co. KGaA, Weinheim

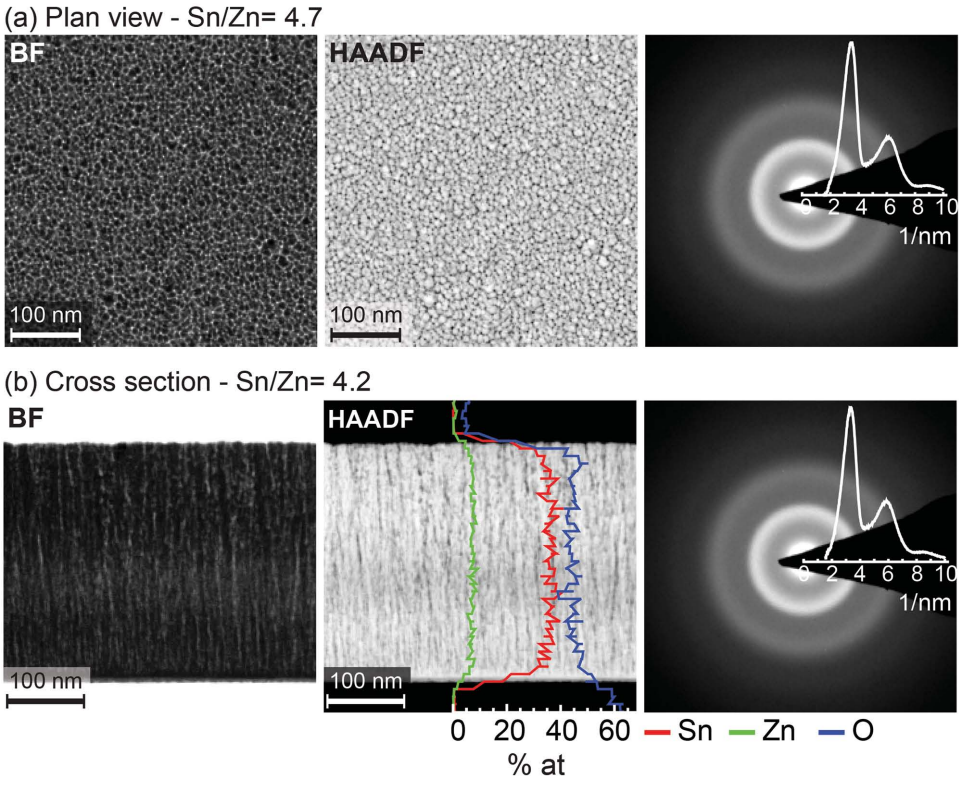

Figure 2. a) STEM BF and HAADF plan view of a cosputtered film with an Sn/Zn ratio of 4.7 along with the corresponding SAED pattern of the film. b) STEM BF and HAADF images, with a STEM EDX line scan of the film superimposed onto the latter image, and SAED pattern of a cross section prepared by FIB.

and it reduces the surface roughness of the films. The thickness of the films is 300 nm in zone 1, and it decreases progressively to 250 nm in zone 5. The large thickness in zone 1 is a result of the higher power density applied to the SnO_2 target. In terms of R_{sh}, the lowest value (240 Ω sq^{-1}) is achieved for the Sn/Zn ratio of 4.3, measured by energy-dispersive X-ray spectroscopy (EDX).

Further optimization of the films with the lowest R_{sh}, i.e., the films with Sn/Zn ≈ 4, was performed by adjusting the power of the SnO_2 and ZnO:Al targets and by cosputtering on a rotating substrate. STEM images, EDX, and SAED analysis of a plan view and a cross section—prepared by conventional focused ion beam (FIB) lift-out technique—of the deposited films are presented in **Figure 2**.

As observed in Figure 2a, when cosputtering with the rotation mode on, the film shows a uniform and smooth surface morphology. Atomic force microscopy (AFM) measurements indicate that the roughness of the films is 1.2 nm RMS (Figure S1, Supporting Information). The small surface "grains" originate from the formation of elongated nanometer-scale voids in the growth direction of the film, as observed in the cross-sectional STEM images (Figure 2b). The formation of voids is a possible effect of the cosputtering deposition. The SAED pattern of both the surface and cross-section clearly shows that the film is amorphous. The cross-sectional EDX line scan shows a uniform distribution of the Zn, Sn, and O elements along the 300 nm thick film. A Sn/Zn ratio of 4.2 was determined from the cross-sectional EDX and confirmed by Rutherford back scattering (RBS).[23]

Hall effect measurements indicate that the films have a free carrier concentration (N_e) of 5×10^{19} cm^{-3} and a Hall mobility (μ_{Hall}) of 12 cm^2 V^{-1} s^{-1}, corresponding to a conductivity (σ) of 110 S cm^{-1} and a resistivity (ρ) of 9×10^{-3} Ω cm. Based on the STEM cross-sectional image, we presume that μ_{Hall} is limited by the presence of voids in the film, creating a potential barrier for the lateral transport of electrons.[23–28] To test this hypothesis, we proceeded to perform the deposition from a single target of ZTO with the composition of Zn = 6.3 at%, Sn = 27.8 at%, and O = 65.9 at%, as determined on the cosputtered films by RBS.

2.2. Optimization of the ZTO Electrodes by Sputtering from a Single Target

A single target of ZTO was fabricated with the composition determined by EDX and RBS from the best cosputtered film (as shown in Figure 2) and used to optimize the optoelectronic properties of the layers as a function of working pressure and oxygen gas flow during sputtering. The sputtering deposition was performed at a base pressure of 1×10^{-3} mbar, keeping a constant flow of argon and varying the oxygen flow at a power density of 2.6 W cm^{-2}.

The electrical properties (ρ, N_e, and μ_{Hall}) as a function of the oxygen flow during sputtering are presented in **Figure 3**. With increasing oxygen flow, N_e decreases, whereas μ_{Hall} increases from 10 cm^2 V^{-1} s^{-1} to a maximum of 18 cm^2 V^{-1} s^{-1} at an

© 2015 WILEY-VCH Verlag GmbH & Co. KGaA, Weinheim

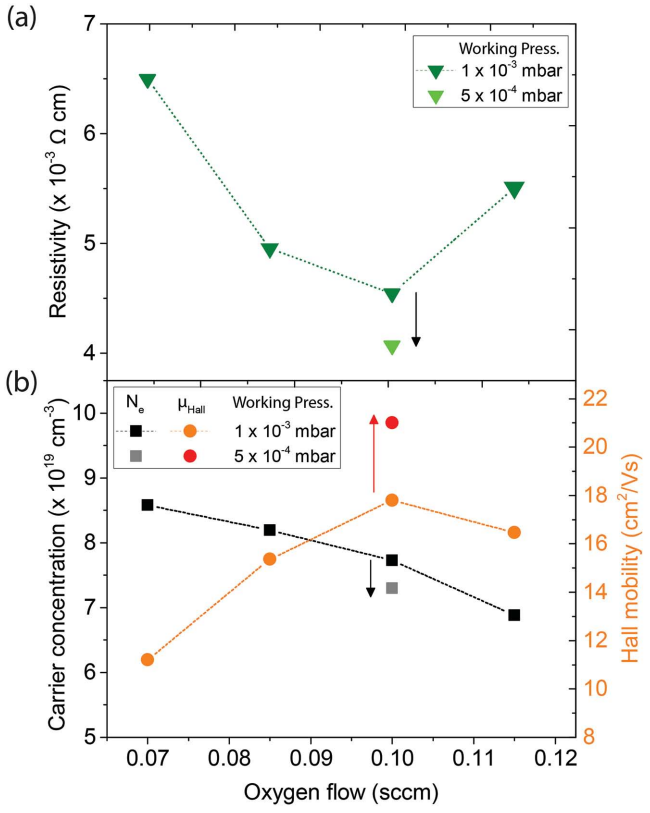

Figure 3. a) Resistivity and b) free carrier concentration and Hall mobility of ZTO films sputtered from a single target as a function of oxygen flow.

oxygen flow of 0.1 sccm. When the oxygen flow is further increased, μ_{Hall} drops slightly to 16 cm^2 V^{-1} s^{-1}. The decrease in N_e with increasing oxygen content can be explained by a reduction of the concentration of oxygen vacancies in the film. It has been reported that, regardless of the microstructure of the films, oxygen vacancies or deficiencies (as they are better described for amorphous materials) are the prevailing sources of charge carriers in ZTO[29,30] as well as other amorphous TCOs.[31,32] The decrease in N_e is compensated with the increase in μ_{Hall}, which possibly occurs due to the lower density of ionized scattering centers in the film.[33]

When reducing the working pressure, from 1×10^{-3} to 5×10^{-4} mbar for the optimal oxygen flow of 0.10 sccm, μ_{Hall} improves to 21 cm^2 V^{-1} s^{-1}, while N_e drops only slightly. The observed improvement in μ_{Hall} with lowering the working partial pressure is described below. Finally, the sheet resistance of the ZTO deposited at low pressure is 266 Ω sq^{-1} for a 150 nm thick film.

Figure 4 presents the optical transmittance and absorptance of the ZTO films sputtered with an oxygen flow of 0.10 sccm for the two working pressures. Both films present excellent optical properties, with >80% average transmittance and <3.5% average absorptance in the visible range (390–700 nm). These properties are in agreement with the optical properties requirements to ensure efficient white-light luminance in OLEDs.[1]

A summary of the electrical properties of the cosputtered and single-target-sputtered films is presented in **Table 1**. In addition, a ZTO film deposited at low pressure and annealed in air at

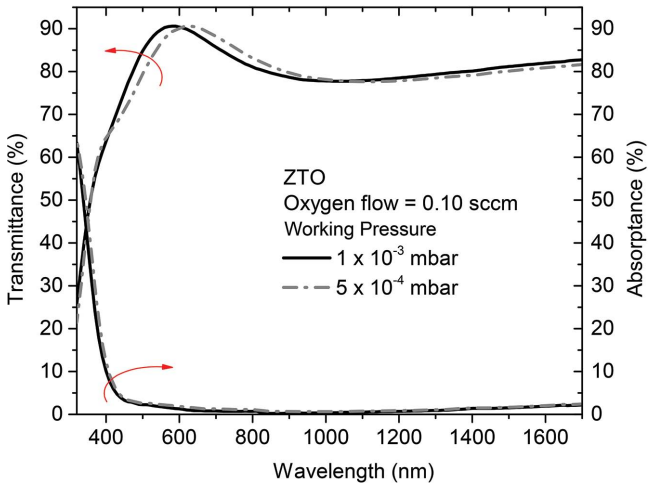

Figure 4. Optical transmittance and absorptance spectra of two ZTO electrodes deposited at two distinct working pressures: 5×10^{-4} and 1×10^{-3} mbar. Both films were fabricated with the same oxygen content.

150 °C for 20 min is listed and it shows a further improvement in conductivity due to an increase in N_e. As observed in Table 1, the N_e of the layers sputtered from a single target is higher than that of the cosputtered film. This higher N_e may be linked to a difference in Sn/Zn ratios between cosputtered and single-target-sputtered films (4.2 and 5, respectively). A larger Sn/Zn ratio hints at a higher density of Sn^{4+} donors in the film, therefore increasing N_e. Following the common explanation for the carrier transport mechanism in amorphous TCOs, electron conduction in these films should be governed by electron transport via Sn 5s–O 2p paths.[34,35]

The microstructure of the as-deposited films summarized in Table 1 was also analyzed by cross-sectional STEM. The images of the films are presented in **Figure 5**.

Cross-sectional STEM images indicate that the void density becomes minimal in films deposited from a single target, and voids are no longer detected in the films deposited with the lowest working pressure (5×10^{-4} mbar).

The formation of voids in sputtered films is a consequence of the interplay between the working pressure of the inert gas (Ar) and oblique deposition during sputtering.[36] Both parameters cause atomic shadowing, i.e., they induce growth at specific points of the films that receive more flux than others, forming open areas. In our case, oblique deposition is a minor effect due to the rotation of the substrate, whereas the working pressure, i.e., flow of Ar gas, plays a major role in the formation of voids in the films.[37,38] This is evident in the formation of dense films with lowering the working pressure of the films as observed in Figure 5.

Based on the STEM observations and because all films have similar N_e values (Table 1), we attribute the improvement in μ_{Hall} for the films deposited at low working pressure to the microstructure, i.e., to the formation of a defect- and void-free layer. In addition to improved μ_{Hall}, the formation of a dense layer is also beneficial for applications in humidity-sensitive devices (e.g., OLEDs), where the dense oxide layer acts as an additional barrier against water ingress.[39]

© 2015 WILEY-VCH Verlag GmbH & Co. KGaA, Weinheim

Table 1. Evolution of the electrical properties of ZTO films from cosputtered films to low-pressure sputtering deposition. Data for an annealed sample are added for comparison.

TCO	Sn/Zn	N_e [cm^{-3}]	μ [$cm^2\ V^{-1}\ s^{-1}$]	ρ [Ω cm]	σ [$\Omega^{-1}\ cm^{-1}$]	R_{sh} [$\Omega\ sq^{-1}$]
ZTO Cosputtered	4.2	5×10^{19}	12	9×10^{-3}	110	600
ZTO single target 1E-3 mbar dep. pressure	5	7.7×10^{19}	18	4.5×10^{-3}	220	300
ZTO single target 5E-4 mbar dep. pressure	5	7.3×10^{19}	21	4×10^{-3}	245	266
ZTO anneal 150 °C	5	9.5×10^{19}	24	2.7×10^{-3}	365	180

The ZTO films also present a low surface roughness of 0.25 nm RMS, determined by AFM in an area of 1 × 1 μm^2 (Figure S1, Supporting Information). This low roughness is an important advantage for the use of ZTO in OLEDs as it avoids possible shunts and leakage current in the devices.[2] Finally, the ZTO films are also chemically stable, i.e., resilient to contact with acids and hence compatible with the entire OLED fabrication process, particularly the lithography step for fabrication of the metal grids.

2.3. Application of ZTO as an Anode in sm-OLEDs

To demonstrate that the developed ZTO anodes are compatible with the sm-OLED fabrication process and to evaluate their performance, we first fabricated small-area devices (5 × 5 cm^2 substrate size, 10 cm^2 active OLED area) on glass. Subsequently, flexible sm-OLED devices on industrial-size substrates (15.2 × 15.2 cm^2) were fabricated on laminated PET foils. Reference devices with ITO were codeposited for comparison in both cases. The process flow of the device fabrication (lamination of the PET substrate on a glass carrier and deposition of the anode and OLED stack) is shown in **Figure 6**. Details of the fabrication process are described in the Experimental Section.

2.3.1. In-Free Small-Area sm-OLEDs

The small area (5 × 5 cm^2 glass substrate) OLED devices were first fabricated to test the compatibility of the developed ZTO as an anode in sm-OLEDs. For this study, only glass substrates were used and no metal grids were applied to the ZTO film (the metal grid fabrication process was optimized only for large-area OLEDs). To achieve an R_{sh} similar to that achieved with ZTO plus metal grids we followed the known approach of introducing a thin silver (Ag) metal layer between two TCO films, in the form: ZTO/Ag/ZTO.[40–42] These ZTO/Ag/ZTO trilayers have an R_{sh} of 9 Ω sq^{-1} and a thickness of 120 nm.

Figure 7 presents the brightness–voltage and luminance efficiency–current density characteristics of an orange sm-OLED device with ZTO/Ag/ZTO anode. The ZTO/Ag/ZTO anode was processed at a temperature of 60 °C, a compatible temperature

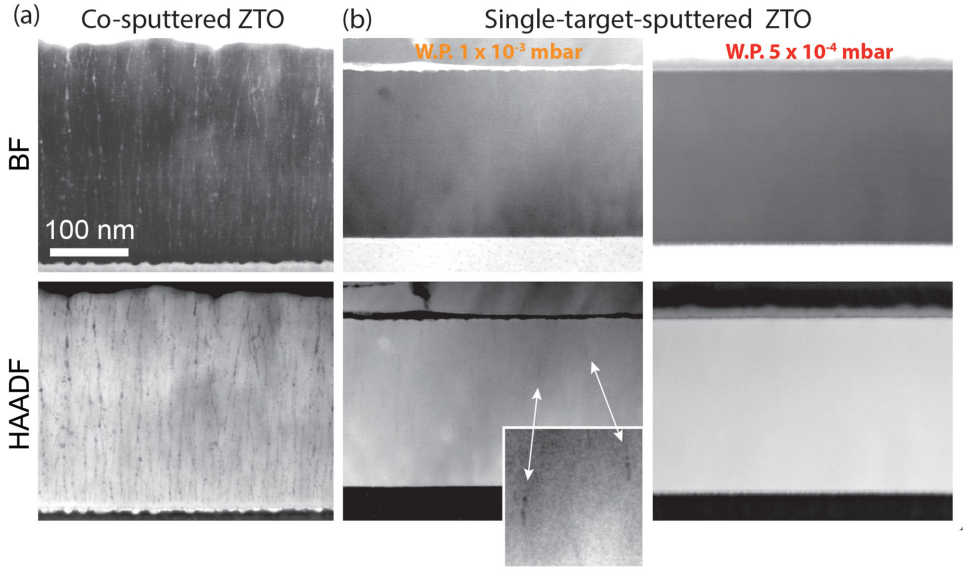

Figure 5. Cross-sectional HAADF and BF STEM images of ZTO thin films deposited by a) cosputtering and b) sputtering from a single ZTO target at two different working pressures (WP). The density of voids in the films is clearly lower for the ZTO sputtered from a single target. Voids are no longer detected in the films deposited at the lowest working pressure. The cross sections of the films were prepared by tripod polishing and low-energy Ar ion milling.

© 2015 WILEY-VCH Verlag GmbH & Co. KGaA, Weinheim

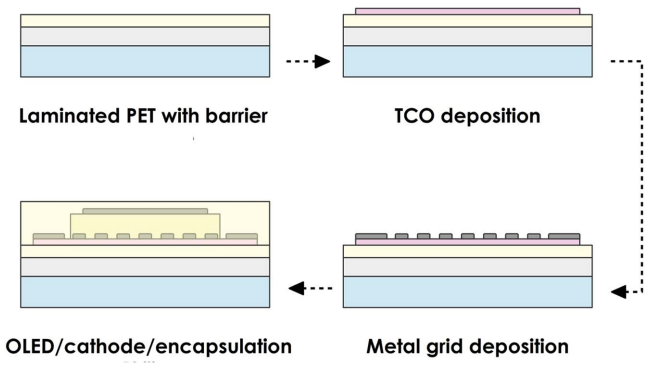

Figure 6. Process flow of sm-OLED fabrication on flexible substrates laminated on a glass carrier

with PET/PEN substrates. These devices are compared to control devices with ITO anodes deposited at high temperatures (>300 °C, not applicable for PET/PEN flexible substrates) and at low temperatures (150 °C, used for PET/PEN substrates). As

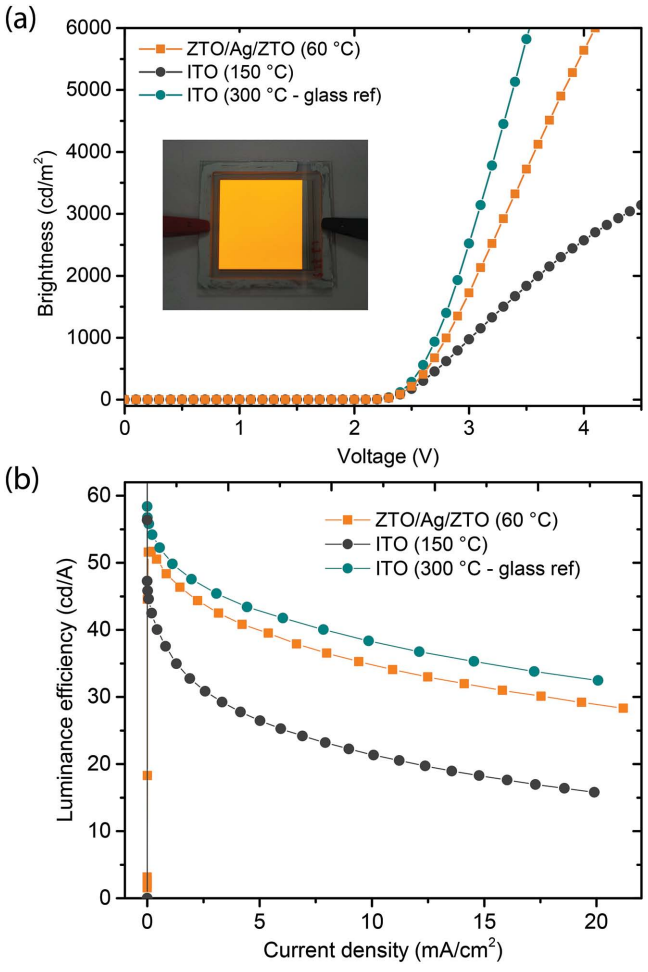

Figure 7. a) Brightness–voltage characteristics and b) luminance efficiency–current density characteristics of orange sm-OLEDs fabricated with ZTO/Ag/ZTO and ITO (deposited at 150 and 300 °C) anodes on 5 × 5 cm² glass substrates. Inset: Picture of one of the orange sm-OLEDs fabricated with ZTO/Ag/ZTO as the anode.

observed in Figure 7a, the sm-OLEDs with ITO deposited at high temperatures show the highest brightness and luminance efficiency, followed by the devices with ZTO/Ag/ZTO. The lowest brightness values are found for the ITO deposited at 150 °C.

The higher brightness and luminance efficiency for the sm-OLEDs with the ITO anode processed at high temperatures (300 °C) is linked to the higher transparency (>80% average in the visible range) as compared to the ZTO trilayer (75% average in the visible range). On the other hand, the lower performance of the low-temperature ITO (processed at 150 °C) might be related to the higher R_{sh} (30 Ω sq^{-1}) as compared to the high-temperature ITO (10 Ω sq^{-1}) and ZTO trilayers (9 Ω sq^{-1}).

Although the high-temperature ITO has the best transparency/conductivity tradeoff, this TCO cannot be applied on flexible PET or PEN substrates, while the ZTO-based electrodes are all deposited at a maximum temperature of 60 °C and are therefore fully compatible with flexible temperature-sensitive substrates. The good performance of the ZTO-based anodes as compared to the low-temperature ITO, as well as the demonstrated compatibility with the OLED fabrication process, indicates the potential for replacing ITO with ZTO as the anode in large-area sm-OLEDs. Also, it is important to mention that ZnO:Al and thin semitransparent metallic layers such as silver constitute an important class of In-free transparent electrodes;[43] however, they are not chemically stable in various solvents and etchants used in processing sm-OLEDs,[13,44,45] reinforcing the importance of the developed chemically stable ZTO anodes.

2.3.2. In-Free Large-Area sm-OLEDs

For the fabrication of sm-OLEDs on 15.2 × 15.2 cm² substrates, the ZTO anodes were deposited onto laminated PET substrates with a thin-film moisture barrier using a shadow mask, forming three 3.5 × 11.5 cm² devices. Subsequently, molybdenum/aluminum/molybdenum (Mo/Al/Mo) hexagonal grids covered with an isolation layer were deposited on top of the ZTO. The isolation layer was used on top of the metal lines to prevent a short circuit of the anode and cathode through the thin organic layers of the OLED.[2] Following these steps, the organic stack was evaporated onto the ZTO/grid anode followed by vacuum deposition of an Al cathode. Devices with the low-temperature ITO plus grid (ITO/grid) were identically fabricated for comparison. Prior to characterization, the devices were delaminated from the glass carrier.

Figure 8a,b shows brightness and luminance efficiency versus current density characteristics of the devices fabricated with ZTO/grid and ITO/grid anode combinations. The current density range corresponds to a voltage sweep from 7 to 10.4 V. As observed in the plots, the device with the ZTO/grid anode shows a slightly higher brightness and luminance efficiency as compared to the device with the ITO/grid. This could be related to lower absorptance of the ZTO films as compared to that of ITO for wavelengths in the visible range. Current density versus voltage curves (Figure 8c) show a slightly lower current in the low-bias region (before turn-on) for the device with ZTO as compared to the device with ITO. Both devices have a turn-on voltage close to 7 V. Even though the ZTO films has a

© 2015 WILEY-VCH Verlag GmbH & Co. KGaA, Weinheim

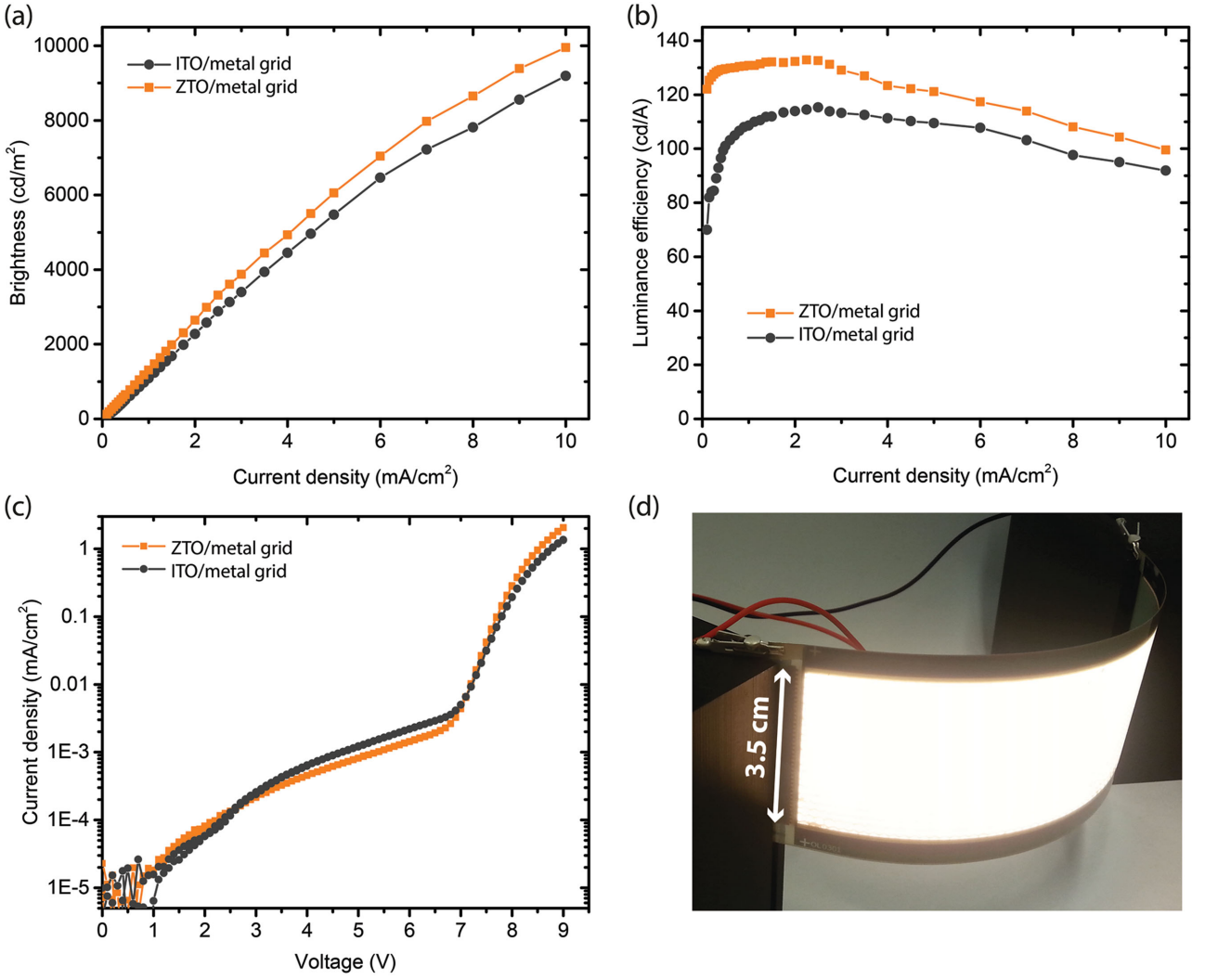

Figure 8. Device performance of white sm-OLEDs fabricated on 15.2 × 15.2 cm^2 PET substrates. a) Brightness versus current density, b) luminance efficiency versus current density, and c) current density versus voltage characteristics for devices with ZTO/grid and ITO/grid anodes. d) Photograph of a curved 3.5 × 11.5 cm^2 sm-OLED device fabricated on the ZTO/grid anode.

higher R_{sh} than the low temperature ITO, the use of the metal grids relaxes the R_{sh} requirements, resulting in excellent device performance for both ITO and ZTO anodes. Figure 8d presents a digital photograph image of a curved operating sm-OLED device fabricated on the ZTO/grid anode.

Shelf-life stability tests performed with large-area red-OLEDs (Supporting Information) indicate that after 480 h, no significant difference between the OLEDs with ITO and ZTO anodes was observed (Figure S4, Supporting Information), confirming that the ZTO/grid anode combination can readily replace the industry-standard ITO/grid anode for large-area sm-OLEDs.

3. Conclusion

We have demonstrated that low-temperature sputtered amorphous ZTO is a viable alternative to ITO in large-area flexible OLEDs. The ZTO films were developed using a combinatorial analysis of ZnO:Al and SnO_2 compositions and by optimizing the optoelectronic properties of films sputtered from a single target with the ideal Sn/Zn ratio. The ZTO films have an optimal combination of low surface roughness, dense amorphous microstructure, good conductivity and excellent optical properties, which are ideal properties for OLED anodes. OLEDs fabricated with ZTO/Ag/ZTO and ZTO/metal (Mo/Al/Mo) grid anodes (fabricated at 60 °C) present better or equal performance to those with low-temperature (150 °C) ITO and ITO/Ag grid anodes, respectively. This, together with the fact that sputtering deposition is a widespread industrial process compatible with large-scale fabrication, clearly demonstrates the feasibility of replacing ITO in actual OLED devices. In addition, the developed ZTO films are composed of only Earth-abundant elements, representing a step forward in the replacement of critical elements such as indium in industrial applications.

© 2015 WILEY-VCH Verlag GmbH & Co. KGaA, Weinheim

4. Experimental Section

4.1. ZTO Films Deposition and Characterization

The ZTO films were deposited by RF sputtering deposition in an Oerlikon Clusterline system. All the films were deposited at a substrate temperature of 60 °C onto a glass substrate (4×8 cm^2) for electrical and optical characterization and onto dedicated transmission electron microscopy (TEM) grids for microstructure characterization. The customized ZTO sputtering target was fabricated by Solar Technology, Inc. For the fabrication of the ZTO/Ag/ZTO trilayers, the deposition time of the ZTO layers was adjusted to achieve 55 nm thick films. The intermediate Ag layer (8 nm thick) was sputtered from an Ag metallic target under an Ar atmosphere at 60 °C. The deposition of the trilayers was performed in a single sputtering chamber.

For the TEM examination, the cross-sections were prepared by either a conventional FIB lift-out technique (Zeiss Nvision) or tripod polishing followed by low-energy argon ion milling (Gatan Pips). Top-view imaging was performed using dedicated 150 nm thick ZTO layers grown on copper grids supporting a thin carbon film. The crystallographic properties of the films were determined by acquiring selected-area diffraction (SAED) patterns, while the structural and chemical assessment of the films involved the acquisition of STEM BF and HAADF images and EDX maps (FEI Tecnai Osiris equipped with four windowless silicon drift detectors for EDX analysis). To complement the EDX results, the chemical composition of the films was also determined by Rutherford backscattering (RBS). Resistivity (ρ), Hall mobility (μ_{Hall}), and free-carrier concentration (N_e) were determined by Hall effect measurements using the van der Pauw configuration. Optical transmittance and reflection spectra in the range of 320–2000 nm were measured using a UV–vis–near infrared (NIR) spectrophotometer equipped with an integrating sphere.

4.2. OLED Devices Fabrication and Characterization

Small area devices: The 5×5 cm^2 glass substrates have been cleaned before OLED deposition. The cleaning procedure involved rinsing in ethanol, brushing with deconex, and an ultrasonic bath in deionized water. The substrates have then been spin-dried before introduction into a Kurt J. Lesker Spectros deposition chamber. A full phosphorescent orange small molecule OLED stack was evaporated at a base pressure of 2×10^{-6} mbar. A 100 nm thick Al layer was evaporated as cathode on top of the organic stack. The surface of the active area measures ≈1000 mm^2. The devices were encapsulated in inert atmosphere with cavity glass lids containing calcium oxide (CaO) getter patches.

Large area devices: The substrate consisted of a foil-on-carrier system, in which a PET plastic foil, with a thin-film moisture barrier on top is temporarily bonded to a glass carrier. The flexible substrate remained attached to the glass carrier during the entire OLED deposition process. On top of the sputtered ZTO electrode, a triple stack of Mo-Al-Mo layers were sputter-deposited and patterned by photolithograpy to form the metal grid (30 µm linewidth) and busbars. A conformal insulator pattern was created using photolithography, resulting in an overhang of 15 µm on either side of the metal lines. The organic layers forming the OLED stack were deposited by thermal evaporation. The OLED stack is a hybrid white sm-OLED stack consisting of a fluorescent (blue) and phosphorescent emitters. An evaporated Al contact was used as the cathode. All the devices were encapsulated using thin-film encapsulation before performing the measurements.

Brightness and current–voltage curves were measured perpendicularly using a combination of a Keithley 2400 Sourcemeter and an LMT 1009 Photometer setup. A voltage sweep of 0 up to 9 V was used to record the characteristic *IV* curves together with the luminance.

Supporting Information

Supporting Information is available from the Wiley Online Library or from the author.

Acknowledgements

This work was funded through the European Union seventh Framework Program (FP7-ICT-2012, Project No. 31462) and by the Swiss National Science Foundation (SNSF) Sinergia project DisCO and Reequipment program. The authors would like to thank S. Nicolay, L. Sansonnens, and J. Fonjallaz from the PV-Center of the Swiss Centre for Electronics and Microtechnology (CSEM) for discussions and technical support. From the Interdisciplinary Centre for Electron Microscopy (CIME) -EPFL, Danièle Laub and Colette Vallotton are acknowledged for STEM sample preparation. The authors are grateful to Duncan MacKerron of Dupont Teijin Films UK Ltd for providing specialized PET substrate films and to Stijn Gillissen of Henkel Electronic Materials NV for supplying the temporary bonding adhesive.

Received: September 4, 2015
Revised: October 1, 2015
Published online: December 10, 2015

[1] S. Reineke, M. Thomschke, B. Lüssem, K. Leo, *Rev. Mod. Phys.* **2013**, *85*, 1245.
[2] J. W. Park, D. C. Shin, S. H. Park, *Semicond. Sci. Technol.* **2011**, *26*, 3.
[3] C. W. Tang, S. A. VanSlyke, *Appl. Phys. Lett.* **1987**, *51*, 913.
[4] M. A. Baldo, D. F. O'Brien, Y. You, A. Shoustikov, S. Sibley, M. E. Thompson, S. R. Forrest, *Nature* **1998**, *395*, 151.
[5] Z. Shen, P. E. Burrows, V. Bulović, S. R. Forrest, M. E. Thompson, *Science* **1997**, *276*, 2009.
[6] M. G. Helander, Z. B. Wang, J. Qiu, M. T. Greiner, D. P. Puzzo, Z. W. Liu, Z. H. Lu, *Science* **2011**, *332*, 944.
[7] Y. Yang, Q. L. Huang, A. W. Metz, J. Ni, S. Jin, T. J. Marks, M. E. Madsen, A. DiVenere, S. T. Ho, *Adv. Mater.* **2004**, *16*, 321.
[8] M.-F. Lo, T.-W. Ng, H.-W. Mo, C.-S. Lee, *Adv. Funct. Mater.* **2013**, *23*, 1718.
[9] R. F. Service, *Science* **2010**, *327*, 1597.
[10] M. C. Gather, A. Köhnen, K. Meerholz, *Adv. Mater.* **2011**, *23*, 233.
[11] X. Jiang, F. L. Wong, M. K. Fung, S. T. Lee, *Appl. Phys. Lett.* **2003**, *83*, 1875.
[12] J. J. Berry, D. S. Ginley, P. E. Burrows, *Appl. Phys. Lett.* **2008**, *92*, 193304.
[13] M. D. L. Olvera, A. Maldonado, R. Asomoza, M. Melendez-Lira, *J. Mater. Sci.: Mater. Electron.* **2000**, *11*, 1.
[14] W. Gaynor, S. Hofmann, M. G. Christoforo, C. Sachse, S. Mehra, A. Salleo, M. D. McGehee, M. C. Gather, B. Lüssem, L. Müller-Meskamp, P. Peumans, K. Leo, *Adv. Mater.* **2013**, *25*, 4006.
[15] L. Zhou, H.-Y. Xiang, S. Shen, Y.-Q. Li, J.-D. Chen, H.-J. Xie, I. A. Goldthorpe, L.-S. Chen, S.-T. Lee, J.-X. Tang, *ACS Nano* **2014**, *8*, 12796.
[16] K. Zilberberg, F. Gasse, R. Pagui, A. Polywka, A. Behrendt, S. Trost, R. Heiderhoff, P. Gorrn, T. Riedl, *Adv. Funct. Mater.* **2014**, *24*, 1671.
[17] M. G. Helander, Z. B. Wang, M. T. Greiner, Z. W. Liu, J. Qiu, *Adv. Mater.* **2010**, *22*, 2037.
[18] O. S. Hutter, H. M. Stec, R. A. Hatton, *Adv. Mater.* **2013**, *25*, 284.
[19] A. Kuruvila, P. R. Kidambi, J. Kling, J. B. Wagner, J. Robertson, S. Hofmann, J. Meyer, *J. Mater. Chem. C* **2014**, *2*, 6940.
[20] N. Li, S. Oida, G. S. Tulevski, S.-J. Han, J. B. Hannon, D. K. Sadana, T.-C. Chen, *Nat. Commun.* **2013**, *4*, 2294.
[21] M. Cai, Z. Ye, T. Xiao, R. Liu, Y. Chen, R. W. Mayer, R. Biswas, K.-M. Ho, R. Shinar, J. Shinar, *Adv. Mater.* **2012**, *24*, 4337.
[22] Z. Chen, Q. Liu, E. Wiedemann, (Hewlett-Packard Dev. Co. Lp.) US20090075421 A1, **2007**.
[23] M. Morales-Masis, L. Ding, F. Dauzou, Q. Jeangros, A. Hessler-Wyser, S. Nicolay, C. Ballif, *APL Mater.* **2014**, *2*, 096113.
[24] K. Ellmer, R. Mientus, *Thin Solid Films* **2008**, *516*, 5829.

© 2015 WILEY-VCH Verlag GmbH & Co. KGaA, Weinheim

[25] J. Y. W. Seto, *J. Appl. Phys.* **1975**, *46*, 5247.
[26] A. W. Metz, J. R. Ireland, J. G. Zheng, R. P. S. M. Lobo, Y. Yang, J. Ni, C. L. Stern, V. P. Dravid, N. Bontemps, C. R. Kannewurf, K. R. Poeppelmeier, T. J. Marks, *J. Am. Chem. Soc.* **2004**, *126*, 8477.
[27] L. Fanni, B. A. Aebersold, D. T. L. Alexander, L. Ding, M. Morales-Masis, S. Nicolay, C. Ballif, *Thin Solid Films* **2014**, *565*, 1.
[28] A. Walsh, J. L. F. Da Silva, S. H. Wei, *Chem. Mater.* **2009**, *21*, 5119.
[29] Q. Zhu, Q. Ma, D. B. Buchholz, R. P. H. Chang, M. J. Bedzyk, T. O. Mason, *J. Appl. Phys.* **2014**, *115*, 033512.
[30] W. Korner, P. Gumbsch, C. Elsasser, *Phys. Rev. B* **2012**, *86*, 165210.
[31] P. D. C. King, T. D. Veal, *J. Phys.: Condens. Matter* **2011**, *23*, 334214.
[32] K. L. Chopra, S. Major, D. K. Pandya, *Thin Solid Films* **1983**, *102*, 1.
[33] A. J. Leenheer, J. D. Perkins, M. F. A. M. van Hest, J. J. Berry, R. P. O'Hayre, D. S. Ginley, *Phys. Rev. B* **2008**, *77*, 115215.
[34] S. C. Siah, S. W. Lee, Y. S. Lee, J. Heo, T. Shibata, C. U. Segre, R. G. Gordon, T. Buonassisi, *Appl. Phys. Lett.* **2014**, *104*, 242113.
[35] T. Kamiya, H. Hosono, *NPG Asia Mater.* **2010**, *2*, 15.
[36] J. A. Thornton, *J. Vac. Sci. Technol., A* **1986**, *4*, 3059.
[37] J. J. Jia, A. Yoshimura, Y. Kagoya, N. Oka, Y. Shigesato, *Thin Solid Films* **2014**, *559*, 69.
[38] V. Assuncao, E. Fortunato, A. Marques, H. Aguas, I. Ferreira, M. E. V. Costa, R. Martins, *Thin Solid Films* **2003**, *427*, 401.
[39] F. So, D. Kondakov, *Adv. Mater.* **2010**, *22*, 3762.
[40] W. Wang, M. Song, T. S. Bae, Y. H. Park, Y. C. Kang, S. G. Lee, S. Y. Kim, D. H. Kim, S. Lee, G. H. Min, G. H. Lee, J. W. Kang, J. Yun, *Adv. Funct. Mater.* **2014**, *24*, 1551.
[41] C. Guillen, J. Herrero, *Thin Solid Films* **2011**, *520*, 1.
[42] N. P. Sergeant, A. Hadipour, B. Niesen, D. Cheyns, P. Heremans, P. Peumans, B. P. Rand, *Adv. Mater.* **2012**, *24*, 728.
[43] K. Ellmer, *Nat. Photonics* **2012**, *6*, 809.
[44] R. G. Gordon, *MRS Bull.* **2000**, *25*, 52.
[45] A. Sharma, B. Kippelen, P. J. Hotchkiss, S. R. Marder, *Appl. Phys. Lett.* **2008**, *93*, 163308.

© 2015 WILEY-VCH Verlag GmbH & Co. KGaA, Weinheim